nature physics

LETTERS

https://doi.org/10.1038/s41567-019-0671-9

Atomic-scale fragmentation and collapse of antiferromagnetic order in a doped Mott insulator

He Zhao[1], Sujit Manna[2,3,4,6], Zach Porter[5], Xiang Chen[5], Andrew Uzdejczyk[1], Jagadeesh Moodera[2,3,4], Ziqiang Wang[1], Stephen D. Wilson[5] and Ilija Zeljkovic[1*]

Disentangling the relationship between the insulating state with a charge gap and the magnetic order in an antiferromagnetic Mott insulator remains difficult due to inherent phase separation as the Mott state is perturbed[1–7]. Measuring magnetic and electronic properties at atomic length scales would provide crucial insight, but this is yet to be experimentally achieved. Here, we use spin-polarized scanning tunnelling microscopy (SP-STM) to visualize the periodic spin-resolved modulations originating from the antiferromagnetic order in a relativistic Mott insulator Sr_2IrO_4 (refs. [8,9]), and how they change as a function of doping. We find that near the insulator-to-metal transition (IMT), the long-range antiferromagnetic order melts into a fragmented state with short-range correlations. Crucially, we discover that the short-range antiferromagnetic order is locally uncorrelated with the observed spectral gap magnitude. This suggests that static short-range antiferromagnetic correlations are unlikely to be the cause of the inhomogeneous closing of the spectral gap and the emergence of pseudogap regions near the IMT. Our work establishes SP-STM as a powerful tool for revealing atomic-scale magnetic information in complex oxides.

A Mott insulator, characterized by localization of electrons due to strong electron–electron interactions[10], is typically accompanied by magnetic ordering[9,11,12]. The antiferromagnetic Mott insulator has been of particular interest as the low-temperature ground state of numerous transition metal oxides[9,11–13], most notably cuprate high-temperature superconductors. Charge carrier doping can gradually suppress this insulating state, a process theoretically expected to lead to inherent phase separation[1,2]. Consistent with this picture of doped Mott insulators, spatially inhomogeneous electronic states, varying on nanometre length scales, have been observed in several systems[3–7]. However, a major experimental failing over the past few decades has been the inability to measure how the antiferromagnetic order evolves over the same length scales, and its relationship to the single-particle gap (charge gap) closing as the Mott state is tuned away from half filling. Spin-polarized scanning tunnelling microscopy (SP-STM) is one of the few available techniques that can in principle be used for atomic-scale imaging of underlying magnetic orders[14]. However, it has so far mostly been applied to magnetic nanostructures[14–17] and Fe-based systems[18,19].

Sr_2IrO_4 (Sr-214) is a quasi-2D layered oxide, in which strong spin–orbit coupling and on-site Coulomb repulsion U lead to the formation of an effective total angular momentum $J_{\mathrm{eff}}=1/2$ Mott state[8,9]. The Mott state is accompanied by an in-plane antiferromagnetic ordering of Ir spins below approximately 240 K (Fig. 1a) and a cooperative in-plane rotation of the IrO_6 octahedra[9], both of which lead to doubling of the primitive unit cell of Ir cations (Fig. 1a,c). Sr-214 doped by electrons is thought to be a nearly perfect analogue to hole-doped cuprates[7,9]. It exhibits many of the same electronic phenomena with doping, such as a pseudogap[5,7,20–22], Fermi arcs[23] and an incommensurate spin density wave[24]. Although superconductivity remains elusive, it has been theoretically predicted to occur at higher electron densities[25]. In contrast to cuprates, where the antiferromagnetic Mott state is suppressed by approximately 0.05 holes per Cu site, the antiferromagnetic Mott state in Sr-214 is only partially quenched even at the highest achievable doping of approximately 0.12 electrons per Ir site[6,26]. Moreover, compared with a relatively large charge gap in insulating cuprates[4,27], a smaller gap in lightly doped, insulating Sr-214 allows tunnelling experiments to be more easily performed[9,28]. As such, this system presents an ideal platform to investigate the interplay of magnetism and electronic correlations within a doped Mott state. Local spectroscopy measurements of electron-doped Sr-214 have provided a glimpse into a spatially inhomogeneous electronic state at low temperature[5,6]. In the lightly doped Mott insulating regime, the Mott gap is pervasive, but as the Mott insulating state is gradually suppressed with increased chemical doping, metallic nanoscale puddles with a V-shape spectral gap begin to nucleate within the insulating background[5,6]. The long-range antiferromagnetic ordering that coexists within the same part of the phase diagram is also progressively suppressed with increased doping[9]. Moreover, there is some experimental evidence suggesting the the long-range antiferromagnetic order may evolve into a short-range antiferromagnetic state near the insulator-to-metal transition (IMT)[6]. In principle, short-range spin correlations could lead to the suppression of the density of states at the Fermi level reflected in a gap-like feature[29], which may be at the root of observed inhomogeneous electronic state. However, as no atomic-scale spin information is available, crucial questions remain: how does the antiferromagnetic order melt with doping, and what is its relationship to the inhomogeneous gap closing and chemical disorder?

To investigate this, we synthesize and study single crystals of $(Sr_{1-x}La_x)_2IrO_4$ (La-doped Sr-214), in which each La substitution contributes approximately one electron to the system. We explore samples in two distinct doping regimes—one deep in the Mott phase with La concentration $x\approx0.02$ and another near the IMT with $x\approx0.05$ (see Methods, Supplementary Fig. 1). Consistent with previous experiments[5,6], a typical STM topograph of our La-doped

[1]Department of Physics, Boston College, Chestnut Hill, MA, USA. [2]Francis Bitter Magnet Laboratory, Massachusetts Institute of Technology, Cambridge, MA, USA. [3]Department of Physics, Massachusetts Institute of Technology, Cambridge, MA, USA. [4]Plasma Science and Fusion Center, Massachusetts Institute of Technology, Cambridge, MA, USA. [5]Materials Department, University of California, Santa Barbara, CA, USA. [6]Present address: Department of Physics, Indian Institute of Technology Delhi, New Delhi, India. *e-mail: ilija.zeljkovic@bc.edu

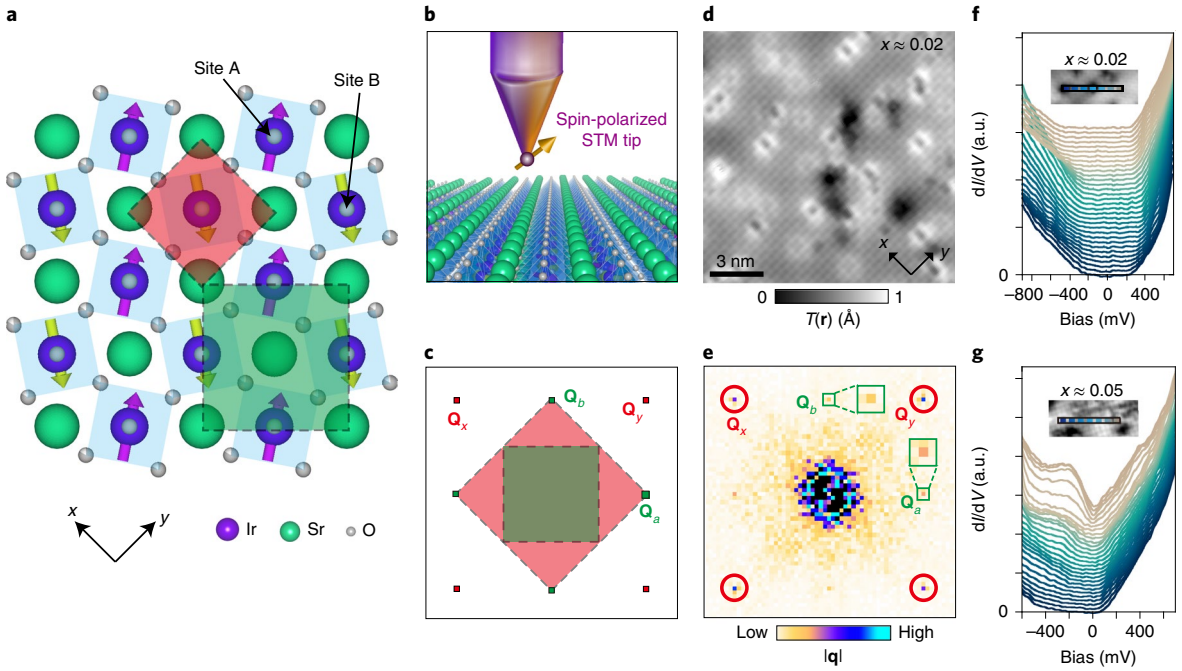

Fig. 1 | Measurement schematic, crystal structure and basic electronic characterization. a, Crystal structure of Sr-214 in the *x*–*y* plane. We show both the Sr lattice unit cell (pink square) and the superstructure unit cell due to IrO_6 octahedral rotation (green square, also magnetic unit cell). The arrows schematically depict spin momenta of Ir atoms. **b**, Schematic of the SP-STM measurement of $(Sr_{1-x}La_x)_2IrO_4$ (La-doped Sr-214). For visualization purposes, the arrow at the apex denotes the spin polarization of the tip. **c**, The expected Fourier transform image of the Sr-214 STM topograph. Pink and green squares correspond to the first Brillouin zone of the Sr lattice and the superstructure, respectively. $\mathbf{Q}_x$ and $\mathbf{Q}_y$ denote the atomic Bragg peaks of the Sr lattice, while $\mathbf{Q}_a$ and $\mathbf{Q}_b$ in principle contain contributions from the octahedral rotation and antiferromagnetic ordering. **d**,**e**, Representative STM topograph of $x \approx 0.02$ La-doped Sr-214 sample (**d**) and its associated Fourier transform obtained using a spin-averaged W tip (**e**). La substitutions are typically visible as bright squares in an STM topograph. **f**,**g**, A series of d*I*/d*V* spectra acquired on the surface of $x \approx 0.02$ (**f**) and $x \approx 0.05$ (**g**) La-doped Sr-214, along the line shown in each inset. STM set-up conditions: bias applied to the sample $V_{sample} = 700$ mV, tunnelling current $I_{set} = 100$ pA, $\mathbf{B} = 0$ T (**d**); $V_{sample} = 700$ mV, $I_{set} = 100$ pA, lock-in excitation $V_{exc} = 5$ mV (zero-to-peak), $\mathbf{B} = 0$ T (**f**); $V_{sample} = 700$ mV, $I_{set} = 250$ pA, $V_{exc} = 8$ mV (zero-to-peak), $\mathbf{B} = 0$ T (**g**).

Sr-214 (which inevitably contains both electronic and structural information) acquired with a spin-averaged W tip reveals a square lattice of Sr atoms in the topmost SrO plane with the lattice constant $a_0 \approx 3.9$ Å (Fig. 1d). In addition to the atomic Bragg peaks $\mathbf{Q}_x = (1,0)$ and $\mathbf{Q}_y = (0,1)$ (we hereafter define reciprocal lattice vector $2\pi/a_0 = 1$), the Fourier transform of the STM topograph also shows peaks at $\mathbf{Q}_a = \left(-\frac{1}{2}, \frac{1}{2}\right)$ and $\mathbf{Q}_b = \left(\frac{1}{2}, \frac{1}{2}\right)$ (Fig. 1e), which were previously hypothesized to be a consequence of the staggered rotation of IrO_6 octahedra[7]. The antiferromagnetic ordering in Sr-214, which has been well established by neutron scattering experiments[6,30], is also spatially modulated with $\mathbf{Q}_a$ and $\mathbf{Q}_b$ wavevectors (Fig. 1a,c), but its signal would be difficult to detect by conventional spin-averaged tunnelling using a W tip. In this work, to achieve spin-resolved imaging, we use spin-polarized STM tips, made from bulk chromium (Cr) wire, trained and characterized on the surface of antiferromagnet $Fe_{1+y}Te$ (see Methods, Supplementary Section 1).

We start with spectroscopic characterization of the $x \approx 0.02$ sample. Consistent with previous work[5], our STM d*I*/d*V* spectra (where *I* is the current and *V* is the voltage applied to the sample) reveal a large insulating U-shaped gap across the entire field of view, which locally decreases in proximity to La dopants (Fig. 1f). Next, we focus on measuring the magnetic signal at $\mathbf{Q}_a = \left(-\frac{1}{2}, \frac{1}{2}\right)$ and $\mathbf{Q}_b = \left(\frac{1}{2}, \frac{1}{2}\right)$. To achieve this, we use a spin-polarized STM tip to acquire STM topographs $T(\mathbf{r},\mathbf{B}_i)$ (where $\mathbf{r}$ is the position vector) of the same region of the sample under varying magnetic field $\mathbf{B}_i \parallel c$ axis, while keeping all other experimental conditions the same. Typically, a spin-polarized tip made from a bulk Cr wire has a canted magnetization direction $\mathbf{P}_{tip}$, with both in-plane and out-of-plane components even at zero magnetic field[14]. By applying an external field $\mathbf{B}_i$, $\mathbf{P}_{tip}$ tilts towards the direction of $\mathbf{B}_i$ (see discussion in Supplementary Section 1). As the direction of $\mathbf{P}_{tip}$ changes, its overlap with the antiferromagnetically ordered spins in the sample also changes, which in turn modulates the measured electronic signal at $\mathbf{Q}_a$ and $\mathbf{Q}_b$. The Fourier transforms of STM topographs obtained using a spin-polarized STM tip show a systematic evolution of $\mathbf{Q}_a$ and $\mathbf{Q}_b$ amplitudes (Fig. 2g). Since nearest neighbour exchange interactions[31] are much stronger than the Zeeman energy at the relatively modest range of fields used in our experiments, we expect no significant change of the antiferromagnetic order of the sample. Thus, the change in $\mathbf{Q}_a$ and $\mathbf{Q}_b$ occurs due to the evolution of the direction of $\mathbf{P}_{tip}$. We note that the Fourier transforms of STM topographs of the same sample acquired using a spin-averaged W tip are nearly identical to one another, and that all Fourier transform peaks remain approximately constant on changing $\mathbf{B}$ (Fig. 2h, Supplementary Section 2). This demonstrates that the change in $\mathbf{Q}_a$ and $\mathbf{Q}_b$ with magnetic field observed with a spin-polarized tip (Fig. 2g) is primarily due to spatially modulated spin-polarized electron tunnelling.

To visualize the spatial distribution of the measured spin-polarized signal, we focus on two topographic images $T(\mathbf{r},\mathbf{B}_1)$ and $T(\mathbf{r},\mathbf{B}_2)$ acquired at different fields over an identical area of the sample (Fig. 2a,b, Methods). As discussed previously, changing the magnetic field from $\mathbf{B}_1$ to $\mathbf{B}_2$ is only expected to affect the direction of $\mathbf{P}_{tip}$ (typically both $\mathbf{B}_1$ and $\mathbf{B}_2$ have the same magnitude but are applied along opposite directions). Then, similarly to the procedure in ref. [18], the difference $M(\mathbf{r}) = T(\mathbf{r},\mathbf{B}_1) - T(\mathbf{r},\mathbf{B}_2)$ yields the spin-resolved magnetic contrast (Fig. 2d), while the average of the two images

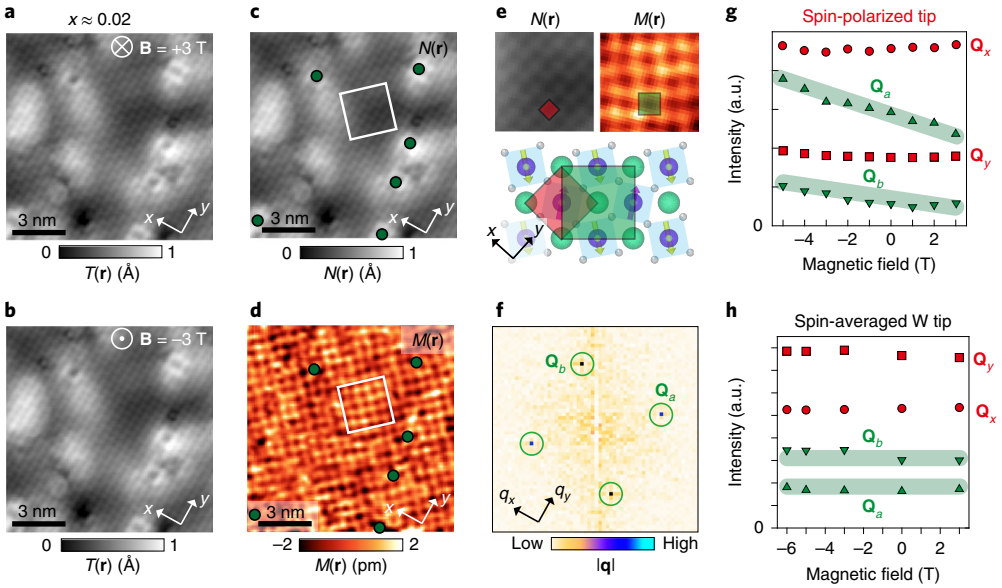

Fig. 2 | Spin-resolved magnetic contrast modulations in lightly doped Sr-214. a,**b**, STM topographs $T(\mathbf{r},\mathbf{B})$ of $x \approx 0.02$ Sr-214 acquired using a spin-polarized tip, in a magnetic field of $\mathbf{B} = +3$ T (**a**) and $\mathbf{B} = -3$ T (**b**) applied perpendicular to the surface (+(−) sign denotes the field applied parallel (antiparallel) to *z*). **c**, $N(\mathbf{r})$ map, defined as the arithmetic average of STM topographs in **a** and **b**. **d**, Spin-resolved magnetic contrast $M(\mathbf{r})$ map, obtained by subtraction of STM topographs in **a** and **b**. Green circles in **c** and **d** denote the locations of La dopants. **e**, Magnification of a small region of the sample outlined by a white square in **c**,**d** showing the atomic-scale structure of $N(\mathbf{r})$ and $M(\mathbf{r})$, as well as the crystal structure of Sr-214. Pink and green squares in **e** denote the Sr unit cell and the superstructure unit cell, respectively. **f**, Fourier transform of $M(\mathbf{r})$ shown in **d**. **g**,**h**, Intensities of Fourier transform peaks extracted from STM topographs $T(\mathbf{r},\mathbf{B})$ acquired over an identical area of the sample in varying magnetic field using a spin-polarized STM tip (**g**) and spin-averaged W tip (**h**). For visual purposes, each pixel in **d** is a boxcar average with the neighbouring eight pixels to smooth over the random noise in the data. We postulate that the difference in the intensity between $\mathbf{Q}_x$ and $\mathbf{Q}_y$ in **g** and **h** at any given field is a consequence of small tip anisotropy. STM set-up condition: $V_{sample} = 700$ mV, $I_{set} = 400$ pA.

$N(\mathbf{r}) = (T(\mathbf{r},\mathbf{B}_1) + T(\mathbf{r},\mathbf{B}_2))/2$ primarily contains non-magnetic electronic information (Fig. 2c). The spin-resolved magnetic contrast image $M(\mathbf{r})$ of the $x \approx 0.02$ sample displays a prominent bi-directional modulation pattern, which is notably absent in the equivalent image obtained on the same sample using a spin-averaged W tip (Supplementary Figs. 4 and 5). The amplitude of the modulations measured in different Sr-214 samples ranges from a few to approximately 10 pm, which is within the range of typical amplitudes of the magnetic signal obtained on other systems[14,15,18,19] (Supplementary Section 2). In the $x \approx 0.02$ sample, the amplitude of spin-resolved modulations in $M(\mathbf{r})$ seems to be spatially homogeneous across the image, unrelated to the local density of La dopants (Fig. 2d, Supplementary Fig. 6). The Fourier transform of $M(\mathbf{r})$ indicates that this is a commensurate order, oriented at 45° with respect to the Sr lattice, with wavevectors narrowly centred on a single pixel at exactly $\mathbf{Q}_a = \left(-\frac{1}{2},\frac{1}{2}\right)$ and $\mathbf{Q}_b = \left(\frac{1}{2},\frac{1}{2}\right)$ (Fig. 2f). This is consistent with the well-established long-range antiferromagnetic order detected by neutron diffraction at this La concentration[6,24]. We note that an STM topograph contains local density of states information from the Fermi level to eV_{sample} (where e is the electron charge and V_{sample} is the bias voltage applied to the sample in the range of 500–700 mV used in this work). Importantly, the $J_{eff} = 1/2$ band is expected to be the only band present in this energy range, as $J_{eff} = 3/2$ is pushed below the Fermi level and other bands are expected at much higher energies[32,33]. This strongly suggests that spin-resolved modulations in $M(\mathbf{r})$ are predominantly associated with the $J_{eff} = 1/2$ band itself.

Next, we repeat the measurement on the $x \approx 0.05$ sample (Fig. 3), which is expected to be close to the IMT[6]. We find that the $M(\mathbf{r})$ image also exhibits two-dimensional modulations (Fig. 3d). However, unlike in the $x \approx 0.02$ sample, we can clearly observe a domain wall (solid line in Fig. 3d, Supplementary Fig. 8), as well as more diffused Fourier transform peaks centred on $\mathbf{Q}_a = \left(-\frac{1}{2},\frac{1}{2}\right)$ and $\mathbf{Q}_b = \left(\frac{1}{2},\frac{1}{2}\right)$, which are no longer contained to a single pixel (Fig. 3f). Furthermore, no new peaks are observable. Interestingly, in some regions of the sample, the modulations appear weaker and even disappear (dashed regions in Fig. 3d), which suggests a wide distribution of local antiferromagnetic strengths (Supplementary Section 2). The observed fragmented state is consistent with a static short-range antiferromagnetic order inferred from transport measurements at this approximate doping[6]. Given that Sr-214 at even higher electron doping should be paramagnetic[6], it is conceivable that the non-ordered regions in $M(\mathbf{r})$ in Fig. 3 could also be paramagnetic. The autocorrelation of $M(\mathbf{r})$ acquired over a larger region of the $x \approx 0.05$ sample (Fig. 4c) gives the correlation length scale of $\xi_{AF} \approx 5$ nm. We can visualize the local strength of magnetic correlations by constructing an amplitude map (Fig. 4d), which highlights the fragmented nature of the state, with ordered puddles varying in size from approximately 10 to greater than 100 IrO_2 plaquettes. We note that intra-unit-cell positions of the modulation peaks in $M(\mathbf{r})$ are centred somewhat away from the Ir site (Fig. 4c), which we attribute to the electron tunnelling path from the IrO_2 plane through the surface SrO layer involving a complex overlap of orbitals and/or possibly O bands mixing into the $J_{eff} = 1/2$ band. To exclude the effects of a particular STM tip and experimental parameters on the observation of the short-range order, we show $M(\mathbf{r})$ images of multiple different samples, acquired using different spin-polarized tips and magnitudes of magnetic fields that exhibit qualitatively the same behaviour (Supplementary Sections 2 and 3). We also repeated the measurement on a related iridate $(Sr_{1-x}La_x)_3Ir_2O_7$ hosting an out-of-plane antiferromagnetic order[9,13], and our SP-STM measurements similarly show a fragmented antiferromagnetic state near the IMT (Supplementary Section 3).

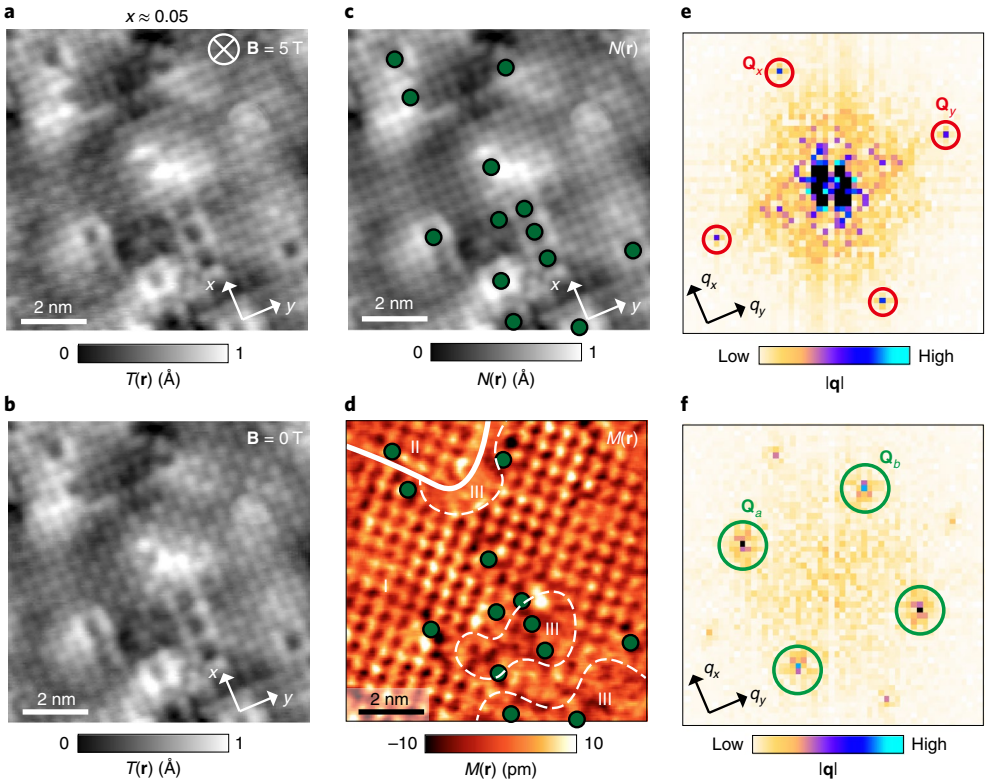

Fig. 3 | Fragmentation of the spin-resolved magnetic contrast modulations at higher electron doping. a,**b**, Scanning tunnelling microscopy (STM) topograph $T(\mathbf{r},\mathbf{B})$ acquired at $\mathbf{B}=5$ T applied perpendicular to the surface (**a**) and $\mathbf{B}=0$ T (**b**) using a spin-polarized tip. **c**, $N(\mathbf{r})$ map, defined as the arithmetic average of STM topographs in **a** and **b**. **d**, Spin-resolved magnetic contrast $M(\mathbf{r})$ map, obtained by the subtraction of images in **a** and **b**. For visual purposes, the image in **d** is separated into three different regions: ordered regions (labelled I and II, offset by a phase) and disordered regions (III) (see Supplementary Fig. 8). Green circles in **c** and **d** denote the locations of La dopants. **e**,**f**, Fourier transforms of images in **c** and **d**, respectively. Relevant Fourier transform peaks in **e** and **f** are denoted by red and green circles. STM set-up condition: $V_{sample}=500$ mV, $I_{set}=300$ pA, $\mathbf{B}=5$ T (**a**); $V_{sample}=500$ mV, $I_{set}=300$ pA, $\mathbf{B}=0$ T (**b**).

We proceed to investigate the relationship between the spatial distribution of the spin-resolved magnetic contrast $M(\mathbf{r})$ and the underlying electronic structure. In accordance with previous spectroscopic measurements of the $x\approx0.05$ sample[5,6], we observe two main types of dI/dV spectra: U-shaped Mott-like spectra similar to those at low doping (blue curve in Fig. 1g) and V-shaped pseudogap-like spectra with a smaller overall gap (grey curve in Fig. 1g). To quantify local electronic structure, we acquire dI/dV spectra on a densely spaced pixel grid and create a map of the approximate gap magnitude $\Delta(\mathbf{r})$ (Fig. 4b, Supplementary Section 4). Theoretical calculations indicate that the opening of the gap in the insulating state should scale with the strength of the antiferromagnetic ordering[32]. In the scenario where the antiferromagnetic state is the only ordered state present, the antiferromagnetically ordered regions would be expected to exhibit larger $\Delta(\mathbf{r})$ and Mott-like spectra, but as the antiferromagnetic order locally weakens and collapses, the gap should also shrink. Therefore, the magnitude of $\Delta(\mathbf{r})$ should strongly correlate with the amplitude of $M(\mathbf{r})$ acquired over the same region of the sample. However, we find that the two observables exhibit no cross-correlation (Fig. 4f). This conclusion can also be confirmed by a visual inspection of Fig. 4a–d, where we can clearly distinguish patches hosting short-range spin-polarized modulations with either a small V-shaped gap (solid blue square) or a large Mott-like gap (solid black square). Similarly, we can also see regions where spin-polarized modulations are absent, but the sample shows either a V-shaped (dashed blue square) or a Mott-like spectrum (dashed black square). This suggests that static short-range antiferromagnetic correlations by themselves are unlikely to be the culprit behind the inhomogeneous gap closing near the IMT.

It remains to be seen which parameter controls the spatial distribution of the short-range antiferromagnetic correlations, as these regions are only weakly correlated (cross-correlation coefficient α ranging between approximately 0 and −0.2) with the distribution of La dopants in the top SrO plane (Fig. 3d, Supplementary Fig. 6). It may be possible that the chemical disorder within the IrO_2 plane or the La dopants in the SrO plane below the top IrO_2 layer have an additional effect on the local amplitude of $M(\mathbf{r})$, but these could not be detected in our experiments. To determine whether the short-range antiferromagnetic domains are pinned by the presence (or absence) of disorder, we propose acquiring $M(\mathbf{r})$ images of the same region of the sample, before and after warming up through the paramagnetic transition. If this experiment finds that these domains shift on thermal cycling, this may present an exciting opportunity to investigate the effect of moving an antiferromagnetic domain on the local electronic structure. Although the inhomogeneous short-range ordering we unveiled does not seem to be tied to the spectral gap variations, it is possible that another ordered state could contribute to these gap modulations, such as a charge density wave[5], or other more exotic possibilities[32,34] (Supplementary Section 6). However, more experiments are necessary to establish connections, if any, between these orders and the inhomogeneous gap closing in this system. Our work provides an insight into how the antiferromagnetic order in a Mott insulator melts with charge carrier doping,

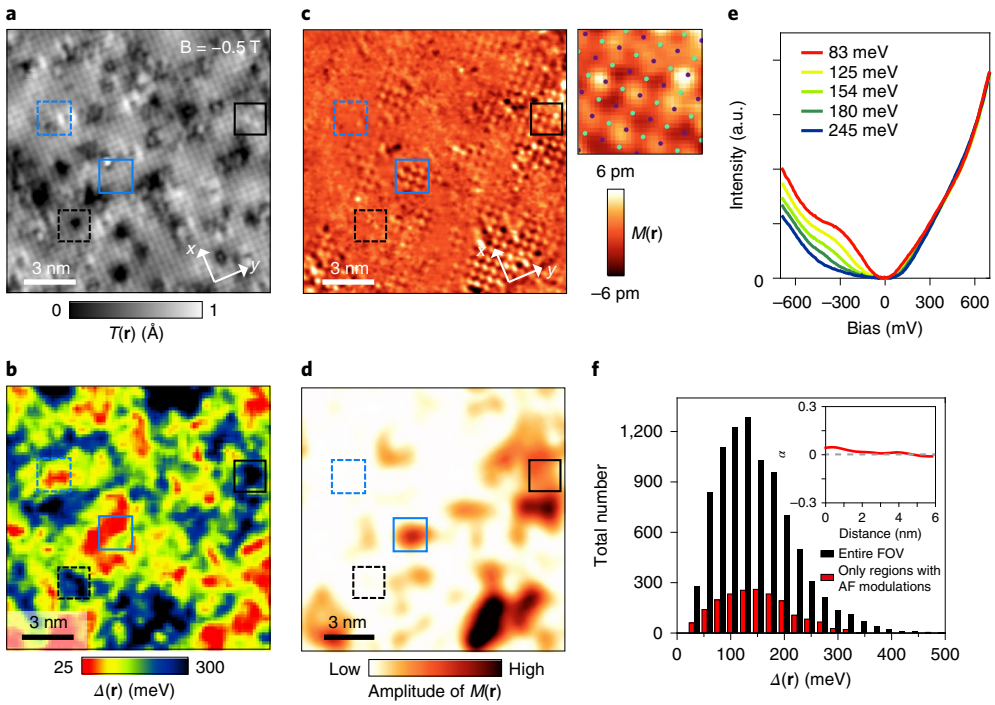

Fig. 4 | Relationship between short-range antiferromagnetic modulations and the electronic structure in $x \approx 0.05$ Sr-214. a–**c**, Scanning tunnelling microscopy topograph $T(\mathbf{r},\mathbf{B}=-0.5\,\mathrm{T})$ (**a**), map of the spectral gap $\Delta(\mathbf{r})$ (**b**) and spin-resolved magnetic contrast map $M(\mathbf{r})$ (**c**), all obtained over an identical region of the sample. The smaller image in **c** is a magnification of the solid black square in **c**, with the approximate locations of Sr (green) and Ir (purple) atoms superimposed on top. **d**, Local amplitude map of $M(\mathbf{r})$. Solid black (blue) squares in **a**–**d** denote regions with spin-resolved modulations and a large (small) gap. Dashed black (blue) squares in **a**–**d** denote regions without spin-resolved modulations and a large (small) gap. **e**, Average dI/dV spectra, binned by the gapmap in **b**, showing a systematic evolution with spectral gap magnitude. The legend in **e** shows the average gap magnitudes within each bin, as determined by the algorithm in ref. [27] and described in Supplementary Section 4. **f**, Histogram of $\Delta(\mathbf{r})$ over the entire field-of-view (FOV) versus the histogram of $\Delta(\mathbf{r})$ in regions with strong antiferromagnetic (AF) spin-resolved modulations only. The inset shows the angularly averaged cross-correlation coefficient α between images in **b** and **d**. STM set-up condition: $V_{\mathrm{sample}} = 700\,\mathrm{mV}$, $I_{\mathrm{set}} = 1\,\mathrm{nA}$.

and establishes SP-STM as a powerful tool to probe magnetism in complex oxides, where spin, charge and orbital degrees of freedom are intertwined at the nanoscale.

Online content

Any methods, additional references, Nature Research reporting summaries, source data, statements of code and data availability and associated accession codes are available at https://doi.org/10.1038/s41567-019-0671-9.

Received: 19 March 2019; Accepted: 23 August 2019;
Published online: 07 October 2019

References

1. Emery, V., Kivelson, S. & Lin, H. Phase separation in the *t*-*J* model. *Phys. Rev. Lett.* **64**, 475–478 (1990).
2. Yee, C.-H. & Balents, L. Phase separation in doped Mott insulators. *Phys. Rev. X* **5**, 021007 (2015).
3. Qazilbash, M. M. et al. Mott transition in VO_2 revealed by infrared spectroscopy and nano-imaging. *Science* **318**, 1750–1753 (2007).
4. Cai, P. et al. Visualizing the evolution from the Mott insulator to a charge-ordered insulator in lightly doped cuprates. *Nat. Phys.* **12**, 1047–1051 (2016).
5. Battisti, I. et al. Universality of pseudogap and emergent order in lightly doped Mott insulators. *Nat. Phys.* **13**, 21–25 (2017).
6. Chen, X. et al. Influence of electron doping on the ground state of $(Sr_{1-x}La_x)_2IrO_4$. *Phys. Rev. B* **92**, 075125 (2015).
7. Yan, Y. J. et al. Electron-doped Sr_2IrO_4: an analogue of hole-doped cuprate superconductors demonstrated by scanning tunneling microscopy. *Phys. Rev. X* **5**, 041018 (2015).
8. Kim, B. et al. Novel $J_{\mathrm{eff}} = 1/2$ Mott state induced by relativistic spin-orbit coupling in Sr_2IrO_4. *Phys. Rev. Lett.* **101**, 076402 (2008).
9. Cao, G. & Schlottmann, P. The challenge of spin–orbit-tuned ground states in iridates: a key issues review. *Rep. Prog. Phys.* **81**, 042502 (2018).
10. Mott, N. F. The basis of the electron theory of metals, with special reference to the transition metals. *Proc. Phys. Soc. A* **62**, 416–422 (1949).
11. Imada, M., Fujimori, A. & Tokura, Y. Metal-insulator transitions. *Rev. Mod. Phys.* **70**, 1039–1263 (1998).
12. Lee, P. A., Nagaosa, N. & Wen, X.-G. Doping a Mott insulator: physics of high-temperature superconductivity. *Rev. Mod. Phys.* **78**, 17–85 (2006).
13. Rau, J. G., Lee, E. K.-H. & Kee, H.-Y. Spin-orbit physics giving rise to novel phases in correlated systems: iridates and related materials. *Annu. Rev. Condens. Matter Phys.* **7**, 195–221 (2016).
14. Wiesendanger, R. Spin mapping at the nanoscale and atomic scale. *Rev. Mod. Phys.* **81**, 1495–1550 (2009).
15. Jeon, S. et al. Distinguishing a Majorana zero mode using spin-resolved measurements. *Science* **358**, 772–776 (2017).
16. Natterer, F. D. D. et al. Reading and writing single-atom magnets. *Nature* **543**, 226–228 (2017).
17. Hirjibehedin, C. F. F., Lutz, C. P. P. & Heinrich, A. J. J. Spin coupling in engineered atomic structures. *Science* **312**, 1021–1024 (2006).
18. Enayat, M. et al. Real-space imaging of the atomic-scale magnetic structure of $Fe_{1+y}Te$. *Science* **345**, 653–656 (2014).
19. Manna, S. et al. Interfacial superconductivity in a bi-collinear antiferromagnetically ordered FeTe monolayer on a topological insulator. *Nat. Commun.* **8**, 14074 (2017).
20. de la Torre, A. et al. Collapse of the Mott gap and emergence of a nodal liquid in lightly doped Sr_2IrO_4. *Phys. Rev. Lett.* **115**, 176402 (2015).
21. Cao, Y. et al. Hallmarks of the Mott-metal crossover in the hole-doped pseudospin-1/2 Mott insulator Sr_2IrO_4. *Nat. Commun.* **7**, 11367 (2016).
22. Kim, Y. K., Sung, N. H., Denlinger, J. D. & Kim, B. J. Observation of a *d*-wave gap in electron-doped Sr_2IrO_4. *Nat. Phys.* **12**, 37–41 (2016).
23. Kim, Y. K. et al. Fermi arcs in a doped pseudospin-1/2 Heisenberg antiferromagnet. *Science* **345**, 187–190 (2014).
24. Chen, X. et al. Unidirectional spin density wave state in metallic $(Sr_{1-x}La_x)_2IrO_4$. *Nat. Commun.* **9**, 103 (2018).

25. Wang, F. & Senthil, T. Twisted hubbard model for Sr_2IrO_4: magnetism and possible high temperature superconductivity. *Phys. Rev. Lett.* **106**, 136402 (2011).
26. Ge, M. et al. Lattice-driven magnetoresistivity and metal-insulator transition in single-layered iridates. *Phys. Rev. B* **84**, 100402 (2011).
27. Zhao, H. et al. Charge-stripe crystal phase in an insulating cuprate. *Nat. Mater.* **18**, 103–107 (2019).
28. Guevara, J. M. et al. Spin-polaron ladder spectrum of the spin–orbit-induced Mott insulator Sr_2IrO_4 probed by scanning tunneling spectroscopy. *Phys. Rev. B* **99**, 121114 (2019).
29. Kyung, B. et al. Pseudogap induced by short-range spin correlations in a doped Mott insulator. *Phys. Rev. B* **73**, 165114 (2006).
30. Ye, F. et al. Magnetic and crystal structures of Sr_2IrO_4: a neutron diffraction study. *Phys. Rev. B* **87**, 140406 (2013).
31. Kim, J. et al. Magnetic excitation spectra of Sr_2IrO_4 probed by resonant inelastic X-ray scattering: establishing links to cuprate superconductors. *Phys. Rev. Lett.* **108**, 177003 (2012).
32. Zhou, S., Jiang, K., Chen, H. & Wang, Z. Correlation effects and hidden spin–orbit entangled electronic order in parent and electron-doped iridates Sr_2IrO_4. *Phys. Rev. X* **7**, 041018 (2017).
33. Solovyev, I. V., Mazurenko, V. V. & Katanin, A. A. Validity and limitations of the superexchange model for the magnetic properties of Sr_2IrO_4 and Ba_2IrO_4 mediated by the strong spin-orbit coupling. *Phys. Rev. B* **92**, 235109 (2015).
34. Zhao, L. et al. Evidence of an odd-parity hidden order in a spin–orbit coupled correlated iridate. *Nat. Phys.* **12**, 32–36 (2016).

Acknowledgements

We thank J. Hoffman, P. Lee and V. Madhavan for valuable discussions, and G. Gu for supplying the FeTe single crystals for characterizing spin-polarized STM tips. The spin-polarized STM measurements were supported by the US Department of Energy Early Career Award DE-SC0020130. I.Z. also acknowledges the support from the Army Research Office grant number W911NF-17-1-0399 (H.Z.) and the National Science Foundation grant number NSF-DMR-1654041 (A.U.) for developing the spin-polarized STM capability. Z.W. acknowledges the support from the US Department of Energy, Basic Energy Sciences grant no. DE-FG02-99ER45747. S.M. and J.M. would like to acknowledge the Office of Naval Research grant N00014-16-1-2657, the National Science Foundation grant DMR-1700137 and a grant from the John Templeton Foundation. S.D.W. acknowledges the support from the National Science Foundation award no. DMR-1905801 (S.D.W.), and additional funding support from the Army Research Office award W911NF-16-1-0361 (Z.P.).

Author contributions

STM experiments were carried out by H.Z. H.Z., S.M. and A.U. were responsible for fabrication and initial characterization of spin-polarized STM tips. Iridate single crystals were grown by Z.P. and X.C., supervised by S.D.W. H.Z. analysed the STM data with guidance from I.Z. Z.W. provided theoretical input on the interpretation of the STM data. I.Z., S.D.W., Z.W., H.Z. and J.M. wrote the manuscript with input from all the authors. I.Z. supervised the project.

Competing interests

The authors declare no competing interests.

Additional information

Supplementary information is available for this paper at https://doi.org/10.1038/s41567-019-0671-9.

Correspondence and requests for materials should be addressed to I.Z.

Peer review information *Nature Physics* thanks Milan Allan and the other, anonymous, reviewer(s) for their contribution to the peer review of this work.

Reprints and permissions information is available at www.nature.com/reprints.

Methods

Single-crystal growth. La-doped Sr-214 single crystals were grown using the flux growth method[6]. The starting powders used were $SrCO_3$ (99.99%, Alfa Aesar), La_2O_3 (99.99%, Alfa Aesar), IrO_2 (99.99%, Alfa Aesar) and anhydrous $SrCl_2$ (99.5%, Alfa Aesar) mixed in a $2(1-x):x:1:6$ molar ratio, where x is the nominal La concentration. They were fully ground, mixed and placed inside a platinum (Pt) crucible, capped by a Pt lid and further protected by an outer alumina crucible. Mixtures were heated slowly to 1,380 °C, soaked for ~5–10 h, slowly cooled to 850 °C over the course of 120 h and then furnace cooled to room temperature over ~5 h. Single crystals used in the work were then obtained after removing excess flux with deionized water. Final bulk concentration of La dopants was determined by using energy-dispersive X-ray spectroscopy (EDX) measurements, and confirmed for each sample by visually counting La dopants in STM topographs (Supplementary Fig. 1).

SP-STM measurements. La-doped Sr-214 samples were cleaved in ultrahigh vacuum at ~80 K and immediately inserted into the STM head. All STM data were acquired at the base temperature of ~4.5 K using a commercial Unisoku USM1300 system. To produce the spin-resolved magnetic contrast $M(\mathbf{r})$ maps, topographic images acquired at two different fields are aligned by applying the Lawler–Fujita drift-correction algorithm[35] and using La dopants as position markers. The Lawler–Fujita algorithm eliminates the inevitable effects of piezo hysteresis and thermal drift, and provides a superior picoscale spatial resolution. Spectroscopic measurements were taken using a standard lock-in technique at 915 Hz frequency and varying bias excitation as detailed in the figure captions.

The STM tips used were homemade, either chemically etched bulk W tips or spin-polarized tips made from bulk Cr wire, as indicated in the figure captions. To obtain an atomically sharp spin-polarized tip, Cr wire (obtained by cutting a ~1-mm-thick Cr sheet into strips, each one with ~1 × ~1 mm^2 cross-section) was etched in 2 mol l^{-1} NaOH solution over the course of 30 min, similar to the procedure described in ref. [36]. Tip sharpness was first evaluated under an optical microscope, before the tip was annealed in an ultrahigh vacuum and inserted into the STM, where its sharpness and spin-polarization was assessed and modified in situ on the surface of ultrahigh-vacuum-cleaved antiferromagnet $Fe_{1+y}Te$ (Supplementary Section 1). We note that a pristine bulk Cr tip is antiferromagnetic, and one may expect that the spin orientation of a Cr tip should remain fixed under different magnetic field. By in situ training and scanning on the surface of $Fe_{1+y}Te$, the Cr tip in our experiments may pick up one or more Fe atoms at the apex. An advantage of spin-polarized tips prepared in this manner is low 'stray' magnetic field because the bulk of the tip is antiferromagnetic, although the apex may contain a small ferromagnetic cluster. We emphasize that our main results are unaffected by the exact details of the evolution of $\mathbf{P}_{tip}$ as a function of magnetic field, as long as the two STM topographs used to calculate an $M(\mathbf{r})$ map are acquired with an STM tip in two different spin states, which can reveal the spin-resolved contrast (more details can be found in Supplementary Section 1).

Data availability

The data represented in Figs. 1f,g, 2g,h and 4e,f are available as Supplementary information files. All other data that support the plots within this paper and the other findings of this study are available from the corresponding author on reasonable request.

Code availability

The computer code used for data analysis is available on request from the corresponding author.

References

35. Lawler, M. J. et al. Intra-unit-cell electronic nematicity of the high-T_c copper-oxide pseudogap states. *Nature* **466**, 347–351 (2010).
36. Huang, D., Liu, S., Zeljkovic, I., Mitchell, J. F. & Hoffman, J. E. Etching of Cr tips for scanning tunneling microscopy of cleavable oxides. *Rev. Sci. Instrum.* **88**, 023705 (2017).